Paramagnon heat capacity in (Ti,Zr,Hf)NiFe$_x$NiSn half-Heusler composites

Trevor P. Bailey [1], Ruiming Lu,[2] Pierre F. P. Poudeu,[2] and Ctirad Uher [1,*]

[1]*Department of Physics, University of Michigan, Ann Arbor, Michigan 48109, USA*
[2]*Laboratory for Emerging Energy and Electronic Materials, Department of Materials Science and Engineering,
University of Michigan, Ann Arbor, Michigan 48109, USA*

As a measure of the temperature response of the energy of matter, the heat capacity C_p is a fundamental thermodynamic property. Its dependence on magnetic field, especially at low temperatures, yields insight into the electronic, phononic, and magnetic states of condensed matter. Here, we present a set of paramagnetic and ferromagnetic (Ti, Zr, Hf)NiFe$_x$Sn half-Heusler composites that exhibit low-field (<3 T) maxima in C_p and higher-field magnetic quenching of the heat capacity at temperatures below 10 K. Using rigorous statistical analysis, we attribute the effect to the existence of paramagnons within the compounds. To explain the lowest-temperature (<4 K), low-field declines in C_p, we derive a magnon model up to fourth order in dispersion. While the combined paramagnon and magnon model matches the data well, the fit parameters are significantly underdetermined. We provide a qualitative explanation of the secondary effect based on superconducting phases within the composites. Overall, our work highlights the insight of field-dependent heat capacity studies at fixed temperatures that cannot be as easily gleaned from the temperature-dependent heat capacity at fixed magnetic fields.

I. INTRODUCTION

The effect of an applied magnetic field H on ground-state thermodynamic properties, including the magnetic susceptibility χ, magnetization M, and heat capacity C_p, has been critical in understanding the condensed-matter physics that enables a wide range of technologies. Prime examples are the magnetocaloric effect for magnetic refrigeration [1–3], single-molecule magnetism for information storage [4,5], and the spin Seebeck effect for spintronics [6,7]. Concerning magnetocalorics specifically, the magnetic contribution to the heat capacity at temperature T, $C_m(H, T)$, is particularly important in calculating the corresponding device figure of merit. $C_m(H, T)$ is also intrinsically tied to the most fundamental models of magnetism in condensed-matter physics, including the classic Heisenberg model [8,9] and the more recent Fermi liquid theory [10]. While studies of $C_m(H, T)$ as a function of temperature are numerous, they often struggle to disambiguate the types of magnetism present in material systems and miss out on the unique response of $C_m(H, T)$ to an applied magnetic field [11]. The rare heat capacity studies that successfully incorporate magnetic fields can be insightful [12–14], but frequently, the underlying physical mechanism is unclear, and the effect is considered to be anomalous [15–20].

To thoroughly explore the dependence of the heat capacity on magnetic field in a range of material systems, we selected a paramagnetic half-Heusler (HH) composite and its mictomagnetic counterparts (paramagnets with secondary phase ferromagnetic $T_C \approx 650$ K) that we recently engineered for thermoelectric applications [21,22]. As a diamagnetic comparison, we also examine the magnetothermodynamics of pure, elemental gold. At low temperatures ($T = 2$ to 10 K), the experimentally measured C_p (heat capacity at constant pressure) in the purely paramagnetic compound features a maximum as a function magnetic field. The mictomagnetic samples additionally display a high-field quenching of the heat capacity. We are able to satisfactorily explain most of the $C_p(H)$ behavior based on paramagnon contributions. However, the paramagnon model cannot account for the low-field heat capacity of the mictomagnetic samples at temperatures lower than 4 K. We therefore derive the magnon contribution with quartic dispersion in field to model the ferromagnetic component of C_p within the mictomagnetic samples. Despite containing only one additional free parameter, the combined paramagnon and magnon model overfits the experimental data. Separate measurements of C_p down to 0.36 K support the paramagnon analysis yet still demonstrate the presence of a separate low-temperature magnetic-field-dependent heat capacity contribution. We qualitatively connect the distinct behavior to a magnetotransport effect witnessed in our previous work [22], namely, the possibility of Sn-based superconducting impurity phases. The $C_p(H)$ trend in the mictomagnetic samples highlights the power of assessing the heat capacity as a function of field at a given temperature compared to the lower sensitivity $C_p(T)$ studies at a given field.

II. EXPERIMENTAL METHODS

Three polycrystalline composites of chemical formula Ti$_{0.25}$Zr$_{0.25}$Hf$_{0.50}$NiFe$_x$Sn$_{0.975}$Sb$_{0.025}$ (TZHNSS), where $x = 0$, 0.05, and 0.10, were synthesized following the procedure

*Corresponding author: cuher@umich.edu

in Ref. [21]. Several 10–20 mg pieces were taken from each fully dense polished ingot in order to conduct the heat capacity measurements. Throughout the text and figures, we commonly refer to the HH samples individually as "HH#", where # is the atomic percentage of Fe included in the compound. Specifically, HH0, HH5, and HH10 refer, respectively, to the 0, 5, and 10 at % Fe-added TZHNSS samples. Pure gold wire of 99.9% purity was purchased from NETZSCH for a diamagnetic comparison.

A Quantum Design physical property measurement system (PPMS) Dynacool model equipped with a 14-T magnet was used for all heat capacity measurements from 0.36 to 400 K. Initial temperature-dependent measurements in zero magnetic field were performed for all samples of the study upon cooling to 2 K. For the 2 to 10 K temperature scans in magnetic field, the chamber was initially set to 2 K to allow the sample holder to stabilize temperature for 2 h. Then, the magnetic field was ramped to a desired value before bringing the temperature to 10 K and waiting a few minutes for temperature stability. The heat capacity was then measured in 1 K increments during cooling, with the temperature stabilized before each measurement. The process was repeated for magnetic fields of 0 to 14 T in fine increments. At each temperature and field, the sample heater was turned on to collect the time-dependent temperature response data $T(t)$. The 2τ modeling of $T(t)$ returned C_p values with less than 5% error. For the heat capacity measurement, a small dab of N grease was first placed on the sapphire sample stage for an addendum measurement without the sample. Once the addendum measurement was complete, an approximately 10–20-mg thin, polished piece of the individual samples was placed on the greased stage for the sample measurement. The difference in C_p between the sample measurement and the addendum yields the C_p of the sample. The same procedure was utilized for the measurement of $C_p(H, T)$ for HH10 down to 0.4 K, with 0.2 K increments used for the in-field scans. The He-3 option of the PPMS, which uses a specially designed sample holder to minimize background noise, addenda values, and addenda field dependence, was needed to achieve such low temperatures. Where appropriate, we normalized $C_p(H, T)$ by the sample mass to yield the specific heat.

III. RESULTS AND DISCUSSION

A. Microstructural properties

A detailed microstructural analysis of the TZHNSS samples can be found in Ref. [21]. We summarize the important aspects here. The TZHNSS samples are composite materials with regions of Ti-rich HH and (Zr, Hf)-rich HH, as indicated by powder x-ray diffraction (PXRD) and scanning electron microscopy. No impurity peaks were detected within the resolution of the PXRD patterns. The chemical compositions and spatial extent of the individual phases are given in Ref. [21]. Transmission electron microscopy unveiled Fe-rich full-Heusler (FH) nanoparticles scattered among the two distinct HH phases. The magnetic FH nanoparticles are of approximate composition $TiNi_{4/3}Fe_{2/3}Sn$, as per electron probe microanalysis. In HH5, the nanoparticles are mainly isolated and $\lesssim 10$ nm in spatial extent. Larger conglomerations of the

Fe-rich phase (up to several hundreds of microns in diameter) are present in HH10.

B. Heat capacity as a function of magnetic field

The magnetic field dependence of the heat capacity for the four samples of the study are displayed in Fig. 1 at temperatures of 2 to 5 K, where the largest-magnitude effects occur. Unlike diamagnetic Au, which features essentially constant $C_p(H)$, the HH samples exhibit starkly nonmonotonic trends of the heat capacity as a function of magnetic field. Specifically, HH0 and HH5 show pronounced peaks in the heat capacities at several teslas, then significant declines in C_p at higher magnetic fields. The maxima contract in magnitude as the temperature is raised while also shifting to larger magnetic field strength. For HH10, the lowest-temperature trends are much different. $C_p(H)$ is fairly flat at 2 K until approximately 2 T, after which it drops precipitously by 50% at 14 T, a $C_p(H)$ quenching equivalent to that of the HH5 sample at 2 K. Similar behavior is seen for HH10 at 3 K, but with a smaller quenching of 35%. At 4 and 5 K, the $C_p(H)$ trends for HH10 mimic those of the other two HH samples, displaying a broad maximum at several teslas with an eventual decline. We stress here that the temperature-dependent C_p at set fields (see Fig. 4 below and Supplementary Material (SM) Fig. S1 [23]) obscure the trends with field in HH0 and show no signs of the unique behavior in HH10, highlighting the sensitivity of $C_p(H)$.

To explain the field dependence of C_p of the three HH samples, we sought out intuitive models that could fit the experimental data with reasonable confidence intervals. Details for the two main models can be found in SM Secs. S1.1 and S1.2, while the fitting procedure and error analysis are elaborated in Sec. S1.3. No modeling was performed for Au since its maximum change in $C_p(H)$ of a mere 1.5% at 2 K is within the addendum $C_p(H)$ limits [Fig. S5(a)]. Because diamagnetic Au displayed no significant $C_p(H)$ effect and paramagnetic phases are a common feature of the HH samples (Refs. [21,22]), the role of paramagnetism in the magnetic-field-dependent heat capacity was a natural first step in our inquiry. Indeed, for HH0, the best-fit minimal model over the whole temperature range is one of multilevel paramagnons (the PM model, for short), which takes on the following form:

$$C_{p,\text{para}} = -n_I k_B y^2 [(2J + 1)^2 \text{csch}^2(2J + 1)y - \text{csch}^2 y]. \quad (1)$$

In Eq. (1), n_I is the concentration of paramagnetic ions, each of total angular momentum J, and $y = \mu_B H/k_B T$ is the ratio of magnetic energy to thermal energy, containing the Bohr magneton μ_B and Boltzmann constant k_B [9]. We allow for the possibility of small internal fields $H_{\text{int,para}}$ within the sample due to the presence of Ni in the compound and the large amount of disorder that can create weak coupling of neighboring spins [14,24,25]. Therefore, $H = H_{\text{int,para}} + H_{\text{ext}}$, with H_{ext} being the magnetic field applied by the PPMS during the experiment. We chose $J = 1/2$ for an electron in an unfilled shell of a bonded atom with quenched orbital momentum [26]. The fitted curves displayed in Fig. 1 capture the structure of $C_p(H)$ with intuitively small internal fields, $H_{\text{int,para}} \approx 1$ T for HH0 and several teslas for the Fe-added
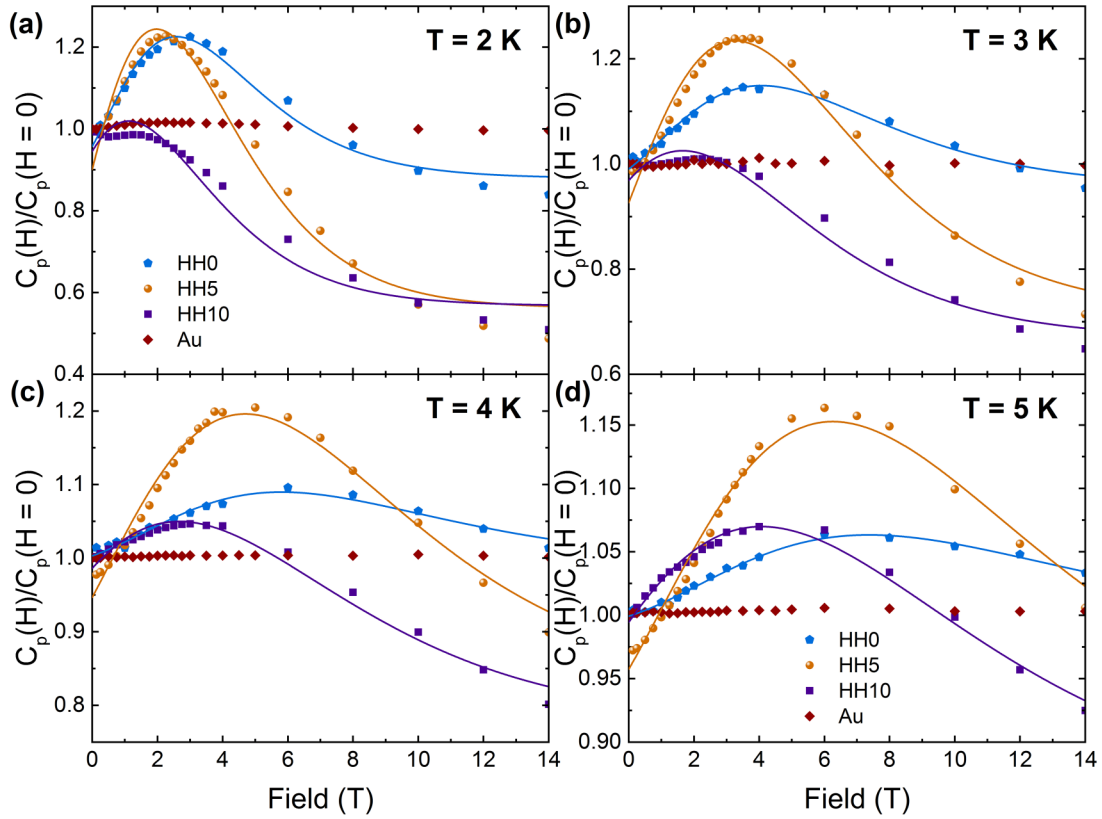
FIG. 1. Magnetic-field-dependent heat capacity of the TZHNSS samples and Au. In (a)–(d), the best-fit curves (solid lines) are least-squares solutions of the experimental data (scattered points) to the paramagnon (PM) model [Eq. (1)] at 2 to 5 K, respectively.

samples. Our statistical analyses in Figs. 2(a) and S3(a)–S3(c) demonstrate reasonable overall confidence intervals for the fit of the PM model to the C_p data of HH0.

The best-fit parameters of the PM model applied to the specific heat of all of the composites are listed in Sec. S1.1, Table S1. For HH0, the number of paramagnetic centers is around 8.5×10^{17} per gram. Based on the molecular weight of the compound ($\approx$300 g/mol), there is approximately one paramagnetic center of strength μ_B for every 2500 unit cells, assuming a homogeneous spatial distribution. For HH5 and HH10, n_I increases by a factor of about 5, meaning that 1 in every 500 f.u. may contain a paramagnetic center. Because none of the constituent elements are at such a low concentration, the $C_p(H)$ effect could stem from trace impurities introduced during the synthesis of the compounds. An alternative explanation is that the phase separation native to these composites naturally hosts unpaired electrons at the grain boundaries, where defects are in abundance. According to our calculation in the SM, Sec. S1.1, attributing all of the paramagnetic centers to a boundary layer approximately 50 unit cells thick would correspond to a paramagnetic center in every fifth unit cell. Such a configuration would maintain the paramagnetic interaction and is consistent with our microscopy [21]. With the data presented here, we cannot discern the paramagnon C_p as sourced solely by trace impurities or the grain boundary defects. Assessing $C_p(H)$ in materials with similar microstructures but different purity reagents in the initial synthesis steps would be one way of understanding the exact cause.

The PM model can capture the $C_p(H)$ behavior fairly well in HH5 at temperatures above 2 K and in HH10 for temperatures above 3 K. However, attempts to fit the $C_p(H)$ data with the PM model at 2 K for the HH5 sample and at 2 and 3 K for HH10 were not as successful as the fitting for HH0 (Figs. 2 and S3). The large confidence intervals of the corresponding fits demonstrate the presence of a separate contribution to $C_p(H)$. Considering that HH5 and HH10 contain ferromagnetic regions in addition to their paramagnetic phases, we believed that magnons could play a role in $C_p(H)$ at the lowest temperatures. We therefore derived the magnon contribution to the heat capacity $C_{p,\text{ferro}}$, as detailed in Sec. S1.2, with the final expression being

$$
\begin{aligned}
C_{p,\text{ferro}} = V T^{\frac{1}{2}} \left(\frac{k_B}{4\pi D} \right)^{\frac{3}{2}} \Bigg\{ & \frac{(g\mu_B H)^2}{k_B T} \mathscr{F}\left(\frac{1}{2}, t_H \right) \\
& + g\mu_B H \left[3 - \frac{5c_1 + 3c_2}{4D}(g\mu_B H) \right] \mathscr{F}\left(\frac{3}{2}, t_H \right) \\
& + \frac{21 k_B T}{2} \left[\frac{5}{14} - \frac{5c_1 + 3c_2}{4D}(g\mu_B H) \right] \mathscr{F}\left(\frac{5}{2}, t_H \right) \\
& + \frac{21(k_B T)^2}{8D}(5c_1 + 3c_2) \mathscr{F}\left(\frac{7}{2}, t_H \right) \Bigg\}.
\end{aligned}
\tag{2}
$$

In Eq. (2), V is the volume of the magnon phase, D is the spin stiffness, g is the unitless Landé spectroscopic splitting factor, and $\mathscr{F}(j, t_H)$ are the Bose-Einstein integrals of order
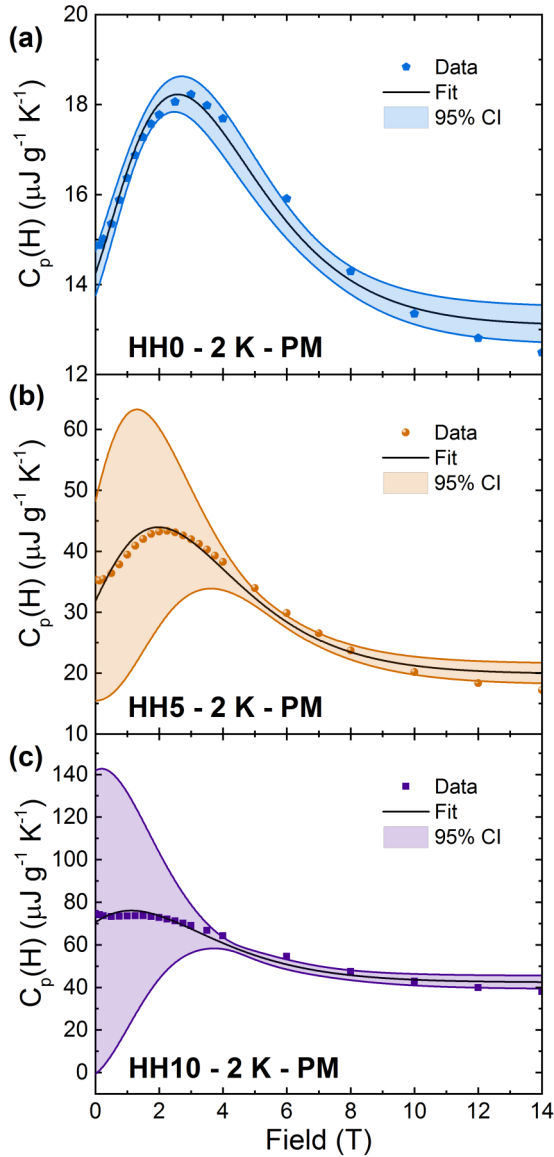
FIG. 2. Paramagnon modeling of the specific heat of the HH composites at 2 K. The best-fit curves (solid black lines) to the experimental data (scattered points) based on the paramagnon (PM) model [Eq. (1)] at 2 K for (a) HH0, (b) HH5, and (c) HH10. The shaded regions with color identical to the data markers are the 95% confidence intervals (CIs).
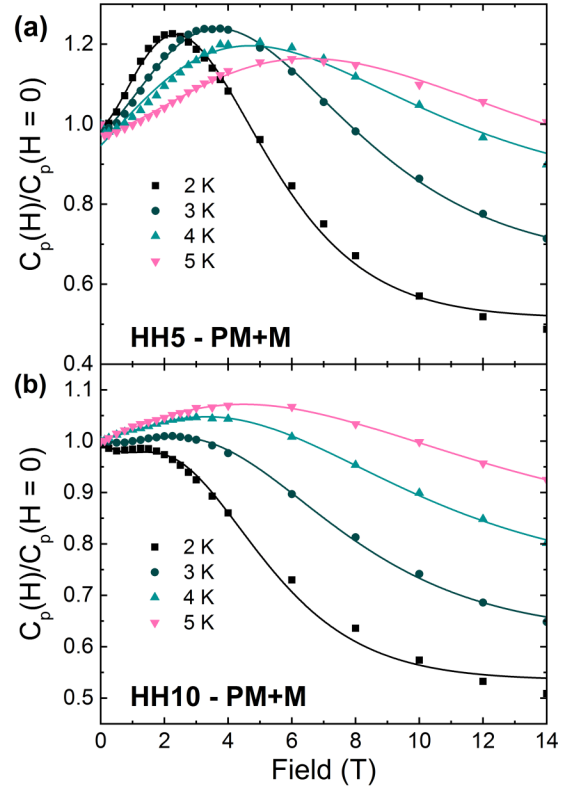

FIG. 3. Magnon modeling of the heat capacity of the Fe-added HH composites. The best-fit curves (solid lines) to the experimental data (scattered points) based on the combined paramagnon and magnon (PM+M) model from 2 to 5 K for (a) HH5 and (b) HH10.

j, defined as

$$\mathscr{F}(j, t_H) = \frac{1}{\Gamma(j)} \int_0^\infty \frac{x^{j-1} dx}{\exp\left(x + t_H^{-1}\right) - 1}, \qquad (3)$$

with $t_H = k_B T / g\mu_B H$ and Γ being the gamma function. Last, the sum $5c_1 + 3c_2$ repeated in Eq. (2) characterizes the quartic dispersion terms of the magnons and is directly related to lattice parameter [27]. The only variable not known, not constant, nor experimentally controlled in $C_{p,\text{ferro}}$ is D, so the combined PM+M (paramagnons and magnons) model contains a single additional free parameter. The best-fit curves of the PM+M model in Fig. 3 match the experimental data quite well. However, our statistical analysis found that the

PM+M model overfits the data, as reflected in the 95% confidence intervals of the magnon fit parameters that span both positive and negative values surrounding the mean value. Overall confidence intervals for the fits of the PM+M model to $C_p(H)$ of HH5 and HH10 were not calculable. Therefore, we cannot rigorously use the PM+M model to explain the additional $C_p(H)$ behavior of HH5 and HH10 at 2 and 3 K. Attempts to fit the data to a spin cluster model [28] as a way of accounting for both the intercluster and intracluster interactions of the magnetic secondary phases in HH5 and HH10 were equally unsuccessful. To entirely eliminate D as a free parameter in the PM+M model, future work could utilize either first-principles calculations or inelastic neutron scattering experiments to assess the spin stiffness of the $\text{TiNi}_{4/3}\text{Fe}_{2/3}\text{Sn}$ phase. That way, the impact of $C_{p,\text{ferro}}(H)$ could be readily determined without any fitting.

To further explore the unique trends of $C_p(H)$ in the Fe-added samples at the lowest temperatures, we measured the specific heat of HH10 down to 0.36 K using the He-3 option of the PPMS. The results are shown in Fig. 4. Although no evident peak as a function of temperature occurs in $C_p T^{-1}$ [Fig. 4(a)] at zero field, the application of a 1-T magnetic field does create a maximum around 0.6 K. The peak shifts to higher temperatures and broadens as larger magnetic fields are applied. Such "Schottky peaks" are described by a generic energy level splitting that can result from nuclear or electronic magnetic moments [9,29,30]. The impact of nondegenerate
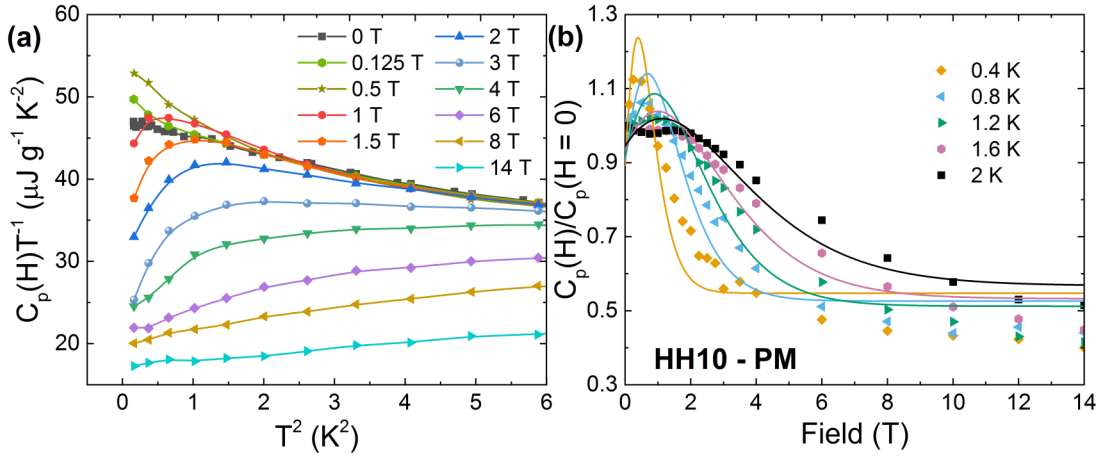
FIG. 4. Specific heat data of HH10 at temperatures below $\approx$2.4 K. (a) $C_p(H)T^{-1}$ against T^2 for HH10 at a number of magnetic fields. The lines are guides to the experimental data points. (b) Normalized heat capacity as a function of magnetic field at several temperatures for HH10 with the best fits of the PM model [Eq. (1)]. Confidence intervals for the fits in (b) are displayed in Fig. S4.

N-level Schottky phenomena on the heat capacity is given by

$$C_{p,Sch} = n_{Sch}k_B \left[\left(\frac{2ye^y}{e^{2y}-1} \right)^2 - \left(\frac{2Nye^{Ny}}{e^{2Ny}-1} \right)^2 \right]$$

$$= n_{Sch}k_B y^2 \left(\mathrm{csch}^2 y - N^2 \mathrm{csch}^2 Ny \right), \qquad (4)$$

which is exactly Eq. (1) with $n_{Sch} = n_I$ and $N = 2J + 1$. Importantly, the presence of the so-called Schottky peak in the temperature-dependent $C_p T^{-1}$ at the lowest temperatures, and its equivalence with the paramagnon perspective, ensures that our analysis of the $C_p(H)$ in terms of the PM model is a correct approach, even for HH5 and HH10 below 4 K.

We plot the normalized best fits to $C_p(H)$ of HH10 at temperatures below 2 K in Fig. 4(b). The corresponding confidence intervals are shown in Fig. S4, while the best-fit parameters are listed in Table S1 of Sec. S1.1. The reemergence of a sharp maximum in the heat capacity as a function of magnetic field at the lowest temperatures is further support that the PM model is appropriate for analyzing $C_p(H)$ since the peak amplitude grows with decreasing temperature. However, the poor fits and large confidence intervals confirm that a separate effect is impacting $C_p(H)$, as we already expected from the 2 and 3 K data. The unique trend of $C_p(H)$ in HH10 at low fields and temperatures is not noticed in the temperature dependence of C_p at set fields (Figs. 4 and S1), highlighting the importance of the field-dependent measurement.

In our previous work [22], we identified a magnetotransport effect in the samples at the lowest temperatures (<4 K) that we attributed to weak antilocalization (WAL). The lowered electrical resistivity required fields of $\approx$1 T at 2 K to return to the normal electronic state, which we argued ruled out the presence of superconducting Sn-based impurity phases that would have superconducting critical temperatures near $T_{C,Sn} \approx 3.7$ K. Looking at the drop in $C_p(H)$ for HH10 at 2 K, we see that it coincidentally stops at around 1 T, after which the expected rise and fall of the PM model kicks in. Furthermore, the inexplicable $C_p(H)$ trend at low fields in HH5 and HH10 occurs only below 4 K, exactly like the magneto-

transport effect. The WAL state heat capacity manifests itself as either a field-dependent electronic contribution, $\gamma(H)T$, or a Schottky-like form [31–33]. In Sec. S1, Fig. S2(a), we demonstrate that γ is mainly independent of magnetic field for all of the samples. Further, the presence of another Schottky-like term, in addition to the paramagnon contribution, would magnify the $C_p(H)$ enhancement with field upon decreasing the temperature from 2 K, contrary to the decline in $C_p(H)$ at low fields and temperatures [Fig. 4(b)].

Elemental superconductors can exhibit enhanced critical fields when their spatial extent is reduced to the nanoscale. For example, indium nanoparticles of diameter <50 nm exhibit critical fields up to $\approx$10 T [34], and similarly sized tin nanowires require fields of $\approx$2 T to return to the normal resistive state at 2 K [35]. In general, cooling through the superconducting transition results in an increased state of heat capacity. Applying magnetic fields in the superconducting state constantly diminishes $C_p(H)$ until it reaches the normal state for $T \lesssim T_C$ [35–37]. Such a decline could account for the low-field behavior of the heat capacity of HH5 and HH10 at temperatures lower than 4 K, where potential Sn-based impurity phases would be superconducting. The simultaneous enhancement of $C_p(H)$ by the paramagnons is offset by the reduction of the superconducting state heat capacity as the magnetic field is applied, resulting in the overall flat low-field trends exemplified by HH10. Although we did not detect any Sn-based impurity phases in the microscopy of the samples [21], it is possible that such nanoscale features could go unnoticed in small concentrations. Because the introduction of Fe adds chemical disorder to the compound and increases the phase separation, Sn-based impurity phases could become more energetically favorable as the alloy demixes. We believe the greater likelihood of Sn-based superconducting impurity phases in HH5 and HH10 could therefore qualitatively explain the unique $C_p(H)$ behavior seen below 4 K.

IV. CONCLUSION

In this paper, we have shown that the magnetic-field-dependent heat capacity $C_p(H,T)$ at low temperatures

(2 to 10 K) is highly sensitive to the presence of para-magnetic centers in a number of magnetically different materials. High-purity, diamagnetic gold displays a mainly constant heat capacity with applied magnetic field, whereas $Ti_{0.25}Zr_{0.25}Hf_{0.50}NiSn_{0.975}Sb_{0.025}$, a highly disordered param-agnetic composite, exhibits a $\gtrsim 20\%$ enhancement in $C_p(H)$ at 2 K under an applied field of 3 T. The peak is gradually suppressed with increasing temperature, essentially vanish-ing above 6 K. We rigorously showed that a two-level paramagnon contribution to the heat capacity can capture the field-dependent behavior. With added iron, the micto-magnetic $Ti_{0.25}Zr_{0.25}Hf_{0.50}NiFe_xSn_{0.975}Sb_{0.025}$ ($x = 0.05$ and 0.10) samples possess tendencies similar to those of the paramagnetic half-Heusler above 3 K. However, at lower temperatures, the confidence intervals of the paramagnon model fits to the experimental data become quite large for the mictomagnetic samples, suggesting a separate magnetic-field-dependent contribution to $C_p(H, T)$. The intuitive magnon model that we derived to explain the additional effect in the partially ferromagnetic samples can mimic the heat ca-pacity trend with one additional free parameter. However, the confidence intervals on the fit parameters indicate that the combined paramagnon+magnon model overfits the data. Separate measurements of the heat capacity of the $x = 0.10$

sample down to 0.36 K confirm our paramagnon analysis and the remaining low-field decline in $C_p(H)$ between 1 and 3 K. We qualitatively link the additional effect to a magneto-transport phenomenon we observed in a previous study, likely stemming from superconducting Sn-based impurity phases that could be present in the composites. Our work illuminates the advantage of studying the magnetic field dependence of C_p at set temperatures, compared to temperature-dependent studies at set fields, in order to witness the totality of under-lying physical phenomena. It would be interesting to further link the analysis here with magnetization and inelastic neutron scattering studies to probe strong paramagnetic systems and ideal ferromagnets.

[1] W. F. Giauque, D. N. Lyon, E. W. Hornung, and T. E. Hopkins, J. Chem. Phys. **37**, 1446 (1962).

[2] V. K. Pecharsky and K. A. Gschneidner, Jr., Phys. Rev. Lett. **78**, 4494 (1997).

[3] V. Franco, J. Blázquez, J. Ipus, J. Law, L. Moreno-Ramírez, and A. Conde, Prog. Mater. Sci. **93**, 112 (2018).

[4] R. Sessoli, D. Gatteschi, A. Caneschi, and M. A. Novak, Nature (London) **365**, 141 (1993).

[5] A. Gaita-Ariño, F. Luis, S. Hill, and E. Coronado, Nat. Chem. **11**, 301 (2019).

[6] K. Uchida, S. Takahashi, K. Harii, J. Ieda, W. Koshibae, K. Ando, S. Maekawa, and E. Saitoh, Nature (London) **455**, 778 (2008).

[7] G. E. W. Bauer, E. Saitoh, and B. J. van Wees, Nat. Mater. **11**, 391 (2012).

[8] W. Heisenberg, Z. Phys. **49**, 619 (1928).

[9] C. Kittel, *Quantum Theory of Solids*, 2nd ed. (Wiley, New York, 1987).

[10] M. Imada, A. Fujimori, and Y. Tokura, Rev. Mod. Phys. **70**, 1039 (1998).

[11] E. Wohlfarth, Phys. B+C (Amsterdam) **91**, 305 (1977).

[12] M. Roy, J. Mitchell, S. Potashnik, and P. Schiffer, J. Magn. Magn. Mater. **218**, 191 (2000).

[13] Y. Onose, T. Ideue, H. Katsura, Y. Shiomi, N. Nagaosa, and Y. Tokura, Science **329**, 297 (2010).

[14] S. C. Riggs, O. Vafek, J. B. Kemper, J. B. Betts, A. Migliori, F. F. Balakirev, W. N. Hardy, R. Liang, D. A. Bonn, and G. S. Boebinger, Nat. Phys. **7**, 332 (2011).

[15] K. Ikeda and K. Gschneider, J. Magn. Magn. Mater. **22**, 207 (1981).

[16] C. Tien, J. J. Lu, and L. Y. Jang, Phys. Rev. B **65**, 214416 (2002).

[17] W. A. Phelan, S. M. Koohpayeh, P. Cottingham, J. W. Freeland, J. C. Leiner, C. L. Broholm, and T. M. McQueen, Phys. Rev. X **4**, 031012 (2014).

[18] S. Yadam, D. Singh, D. Venkateshwarlu, M. K. Gangrade, S. S. Samatham, and V. Ganesan, Bull. Mater. Sci. **39**, 537 (2016).

[19] A. K. Mishra, M. Krishnan, D. Singh, S. S. Samatham, M. Gangrade, R. Venkatesh, and V. Ganesan, J. Magn. Magn. Mater. **448**, 130 (2018).

[20] F. Kneidinger, I. Zeiringer, A. Siderenko, E. Bauer, H. Michor, P. Rogl, and J. G. Sereni, Phys. Rev. B **100**, 134442 (2019).

[21] R. Lu, J. S. Lopez, Y. Liu, T. P. Bailey, A. A. Page, S. Wang, C. Uher, and P. F. P. Poudeu, J. Mater. Chem. A **7**, 11095 (2019).

[22] T. P. Bailey, R. Lu, P. Poudeu, and C. Uher, Mater. Today Phys. **11**, 100155 (2019).

[23] See Supplemental Material at http://link.aps.org/supplemental/10.1103/PhysRevB.102.224412 for model details, the fitting procedure, error analysis, PPMS calibration, and data repro-ducibility, which includes Refs. [38–42].

[24] S. Kim, R. Fisher, N. Phillips, and J. Gordon, Phys. C (Amsterdam, Neth.) **162–164**, 494 (1989).

[25] J. Loram, K. Mirza, and P. Freeman, Phys. C (Amsterdam, Neth.) **171**, 243 (1990).

[26] E. Roduner, Phys. Chem. Chem. Phys. **20**, 23812 (2018).

[27] F. Keffer, in *Ferromagnetism/Ferromagnetismus*, edited by H. P. J. Wijn (Springer, Berlin, 1966), pp. 1–273.

[28] K. Levin and D. L. Mills, Phys. Rev. B **9**, 2354 (1974).

[29] E. Gopal, *Specific Heats at Low Temperatures* (Plenum, New Delhi, 1966).

[30] R. L. Falge and N. M. Wolcott, J. Low Temp. Phys. **5**, 617 (1971).

[31] P. A. Lee and T. V. Ramakrishnan, Rev. Mod. Phys. **57**, 287 (1985).

[32] H. Kamimura and E. Yamaguchi, Solid State Commun. **28**, 127 (1978).

[33] N. Kobayashi, S. Ikehata, S. Kobayashi, and W. Sasaki, Solid State Commun. **32**, 1147 (1979).

[34] W.-H. Li, C. C. Yang, F. C. Tsao, S. Y. Wu, P. J. Huang, M. K. Chung, and Y. D. Yao, Phys. Rev. B **72**, 214516 (2005).

[35] Y. Zhang, C. H. Wong, J. Shen, S. T. Sze, B. Zhang, H. Zhang, Y. Dong, H. Xu, Z. Yan, Y. Li, X. Hu, and R. Lortz, Sci. Rep. **6**, 32963 (2016).

[36] G. Mu, H. Luo, Z. Wang, L. Shan, C. Ren, and H.-H. Wen, Phys. Rev. B **79**, 174501 (2009).

[37] Y. Bang and G. R. Stewart, J. Phys.: Condens. Matter **29**, 123003 (2017).

[38] J. Kouvel and H. Brooks, *Some Spin Wave Properties of Ferrimagnetic and Antiferromagnetic Simple Cubic Crystals*, U.S. Office of Naval Research Technical Report 198 (Harvard University, Cambridge, MA, 1954).

[39] M. F. Collins, V. J. Minkiewicz, R. Nathans, L. Passell, and G. Shirane, Phys. Rev. **179**, 417 (1969).

[40] *Physical Property Measurement System: Heat Capacity Option User's Manual* (Quantum Design, San Diego, CA, USA, 2014).

[41] J. Lashley, M. Hundley, A. Migliori, J. Sarrao, P. Pagliuso, T. Darling, M. Jaime, J. Cooley, W. Hults, L. Morales, D. Thoma, J. Smith, J. Boerio-Goates, B. Woodfield, G. Stewart, R. Fisher, and N. Phillips, Cryogenics **43**, 369 (2003).

[42] B. Boerstoel, J. Zwart, and J. Hansen, Physica **54**, 442 (1971).